

Demonstration of high-performance negative central magnetic shear discharges in the DIII-D tokamak*

B. W. Rice,^{†,a)} K. H. Burrell, L. L. Lao, G. Navratil,^{b)} B. W. Stallard,^{a)} E. J. Strait, T. S. Taylor, M. E. Austin,^{c)} T. A. Casper,^{a)} M. S. Chu, C. B. Forest, P. Gohil, R. J. Groebner, W. W. Heidbrink,^{d)} A. W. Hyatt, H. Ikezi, R. J. La Haye, E. A. Lazarus,^{e)} Y. R. Lin-Liu, M. E. Mauel,^{b)} W. H. Meyer,^{a)} C. L. Rettig,^{f)} D. P. Schissel, H. E. St. John, P. L. Taylor, A. D. Turnbull, and the DIII-D Team

General Atomics, P.O. Box 85608, San Diego, California 92186-9784

(Received 9 November 1995; accepted 7 February 1996)

Reliable operation of discharges with negative central magnetic shear has led to significant increases in plasma performance and reactivity in both low confinement, L-mode, and high confinement, H-mode, regimes in the DIII-D tokamak [*Plasma Physics and Controlled Nuclear Fusion Research 1986* (International Atomic Energy Agency, Vienna, 1987), Vol. 1, p. 159]. Using neutral beam injection early in the initial current ramp, a large range of negative shear discharges have been produced with durations lasting up to 3.2 s. The total noninductive current (beam plus bootstrap) ranges from 50% to 80% in these discharges. In the region of shear reversal, significant peaking of the toroidal rotation [$f_{\phi}(0) \sim 30\text{--}60$ kHz] and ion temperature [$T_i(0) \sim 15\text{--}22$ keV] profiles are observed. In high-power discharges with an L-mode edge, peaked density profiles are also observed. Confinement enhancement factors up to $H \equiv \tau_E/\tau_{ITER-89P} \sim 2.5$ with an L-mode edge, and $H \sim 3.3$ in an edge localized mode (ELM)-free H mode, are obtained. Transport analysis shows both ion thermal diffusivity and particle diffusivity to be near or below standard neoclassical values in the core. Large pressure peaking in the L mode leads to high disruptivity with $\beta_N \equiv \beta_T/(I/aB) \leq 2.3$, while broader pressure profiles in the H mode gives low disruptivity with $\beta_N \leq 4.2$. © 1996 American Institute of Physics. [S1070-664X(96)94805-6]

I. INTRODUCTION

The development of a tokamak plasma with good magnetohydrodynamic (MHD) stability properties while maintaining high confinement, high β_T ($\beta_T \equiv \langle p \rangle 2\mu_0/B_T^2$, where $\langle p \rangle$ is the volume averaged pressure and B_T is the toroidal field), and a large fraction of noninductive bootstrap current, is an essential step toward making the tokamak a more attractive energy source.^{1,2} It has been proposed that a plasma discharge with negative central magnetic shear (NCS) may meet these objectives [magnetic shear is defined as $S = (2V/q)(dq/dV)$, where q is the safety factor and V is the flux surface volume]. NCS discharges hold the promise of simultaneously achieving improved stability to high- n ballooning modes due to second stability access in the core and a bootstrap current density profile that is well aligned with the total (hollow) current density profile $J(r)$. Numerical simulations³⁻⁵ indicate that this configuration can be maintained in steady state at high normalized beta [$\beta_N \equiv \beta_T/(I/aB_T)$, where I is the plasma current and a is the minor radius] and large bootstrap fraction with a small amount of additional localized noninductive current drive. Calculations also show that negative magnetic shear is stabilizing for trapped particle drift-type microinstabilities,⁵⁻⁷

which are a leading candidate for the anomalous transport observed in tokamaks. Thus, reduced transport is expected in the region of shear reversal.

Long-wavelength MHD stability to ideal kink and infernal modes, as well as various resistive modes, is not guaranteed in the NCS configuration and must be evaluated carefully for given pressure and q profiles. For example, in simulations^{3,4} it is found that at high β_N , stability to low- n kink modes requires stabilization from an external conducting shell under conditions of continued plasma rotation. Stability to resistive double tearing modes, which arise with nonmonotonic q profiles, may require stabilization through strong plasma flow shear.⁸

There is mounting experimental evidence that both stability and confinement properties are improved in plasma discharges with NCS. Many early experiments reported peaking of the central pressure,⁹⁻¹² implying an internal transport barrier. In most of these cases, however, the evidence for NCS was indirectly inferred due to the lack of detailed poloidal field measurements. Improved stability in NCS has also been shown previously on DIII-D,¹³ where $\beta_T(0) = 44\%$ and $\beta_T = 11\%$ was achieved in a negative shear configuration.⁹ NCS discharges with strong density and pressure peaking have also been reported recently on the Tokamak Fusion Test Reactor, TFTR.¹⁴

The recent development of inductive and noninductive techniques to shape the q profile, and accurate diagnostics to measure the q profile, has led to controlled experiments to study the confinement and stability of NCS discharges with high-confinement (H-mode) and low-confinement (L-mode) edge conditions in DIII-D. In these experiments, the inverted

*Paper 5IA4, Bull. Am. Phys. Soc. **40**, 1747 (1995).

[†]Invited speaker.

^{a)}Lawrence Livermore National Laboratory, Livermore, California 94551.

^{b)}Columbia University, New York, New York 10027.

^{c)}University of Maryland, College Park, Maryland 20742.

^{d)}University of California, Irvine, California 92717.

^{e)}Oak Ridge National Laboratory, Oak Ridge, Tennessee 37831.

^{f)}University of California, Los Angeles, California 90024.

q profile is established using neutral beam injection in the co-current direction early in the initial current ramp.¹⁵ Although current profiles produced in this manner are transient (evolving toroidal electric field), typical current diffusion times are ~ 10 s, so the inverted q profile can generally be maintained for the duration of the experiment (~ 4 s) on DIII-D. This is adequate for studying the transport and stability properties of the NCS configuration.

Initial NCS experiments using early beam injection in DIII-D in the edge-localized mode (ELM)-free H mode¹⁶ obtained confinement enhancement factors $H \equiv \tau_E / \tau_{\text{ITER-89P}} \sim 3.3$ (τ_E is the energy confinement time and $\tau_{\text{ITER-89P}}$ is the ITER L-mode scaling law¹⁷) and $\beta_N \sim 4$. Significant peaking of the central ion temperature [$T_i(0) \sim 15$ – 20 keV] and toroidal rotation [$f_\phi(0) \sim 50$ kHz] inside the minimum q (q_{min}) radius was observed. In NCS discharges that maintain an L-mode edge,¹⁸ $H=2.5$ and $\beta_N=2.3$ were reported, and peaking of T_i , f_ϕ , and electron density n_e was observed inside the radius of q_{min} . At the time, these discharges produced the record deuterium (DD) neutron rates Γ_n on DIII-D.

The purpose of this paper is to provide an overview of the NCS experimental results on DIII-D, including recent experiments, to present results from transport and stability analysis, and to propose a path for future research. The emphasis will be on comparing NCS results in the L and H mode, which have significantly different density, pressure, and beam deposition profiles, to determine the advantages and disadvantages of each regime. The paper is organized as follows. In Sec. I we describe the formation of a long pulse ELMing H mode and high-performance L- and H-mode NCS discharges, illustrating the temporal evolution and profiles for typical discharges. In Sec. II we discuss bootstrap current profiles and alignment. Transport analysis is presented in Sec. III, and the stability of NCS discharges is discussed in Sec. IV. We conclude with a summary of the achievements in NCS discharges and discuss plans for future research. Further analysis of transport and stability of these discharges is presented in a companion paper by Lao *et al.*¹⁹

All discharges described in this paper were performed in a double-null configuration with elongation ~ 2 and triangularity ~ 0.85 . The beam and neutral gas fueling is deuterium, and the normal beam energy is 75 keV. The toroidal field is 2.1 T unless indicated otherwise.

II. PROFILE EVOLUTION IN NCS DISCHARGES

NCS discharges are produced on DIII-D using codirectional neutral beam injection early in the initial current ramp.¹⁵ A low target density of 1 – 1.5×10^{19} m⁻³ gives high central electron temperatures of $T_e(0) \sim 4$ keV early in the current ramp. Characteristic core current diffusion times are ~ 4 s with early beam injected power P_{nbi} compared to 0.3 s without. Thus, early P_{nbi} effectively freezes in $J(0)$ at a low value, forcing a hollow current density profile to develop as the plasma current ramps up. Off-axis beam and bootstrap currents additionally reinforce the inverted q profile.

Some degree of shot-to-shot control of $q(r)$ is obtained by varying target density, early beam power, and timing. Using these techniques, q profiles with $2 \leq q_0 \leq 10$, $1 \leq q_{\text{min}} \leq 3$, and $0.2 \leq \rho_{q_{\text{min}}} \leq 0.75$ can be obtained (ρ is an effective radius

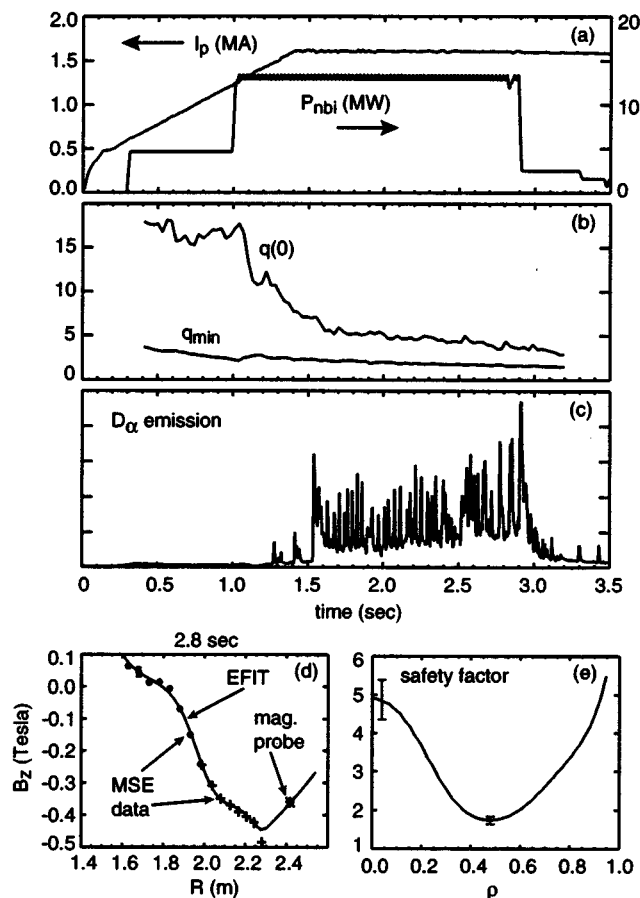


FIG. 1. Time evolution of (a) I_p, P_{nbi} ; (b) q_0, q_{min} ; and (c) D_α emission for discharge 83724, illustrating that the NCS configuration (indicated by $q_0 > q_{\text{min}}$) produced by early beam injection can be maintained for long pulses in an ELMing H mode. The vertical field and q profiles at 2.8 s determined from EFIT with MSE data are shown in (d) and (e), respectively.

defined as the square root of the toroidal flux normalized to the value at the separatrix, and $\rho_{q_{\text{min}}}$ is the radius of minimum q). Programming an H-mode transition during the current ramp is especially effective at raising the edge temperature and hence broadening the $J(r)$ profile giving higher q_{min} , larger $\rho_{q_{\text{min}}}$, and lower internal inductance, l_i .

To sustain inverted q profiles produced in this manner for long pulses requires long L/R times, low MHD activity, and a reasonably well-aligned bootstrap current profile. These criteria are satisfied in the ELMing H-mode NCS discharge shown in Fig. 1, where negative central shear is maintained for the duration of the beam heating phase. Here, 5 MW of beam power is injected at 0.3 s into the initial current ramp, generating the early inverted q profile. A higher-power (13 MW) phase begins at 1.0 s, still during the current ramp. A short ELM-free period is followed by an ELMing H mode, which lasts until the beam power is shut off at 3.2 s. Profiles of q are determined by EFIT²⁰ with MSE measurements^{21,22} of the internal field pitch angle profile. From the time history of $q(0)$ and q_{min} shown in Fig. 1(c), we see that the q profile is inverted and, during the I_p flat top, evolving slowly. The MSE vertical field B_z measurements and corresponding q profile are shown for a time slice at 2.8 s just prior to the end

of beam heating. The flattening of the poloidal field near the magnetic axis seen in the MSE data is characteristic of the hollow current density profile. Typical error bars on q_{\min} and $q(0)$ are also shown.

The key to the longevity of this NCS discharge is the avoidance of MHD. Once ELMing begins, this discharge is otherwise free from MHD activity. The ELM-free period is relatively short due to the high P_{nb}^{L} phase beginning during current ramp at 1.0 s, which is earlier than usual NCS discharges, where the high-power phase might begin between 1.5–2.0 s. The short ELM-free period prevents a large increase in stored energy and subsequent β collapse that often follows. The calculated noninductive beam and bootstrap current is approximately 50% of the total in this discharge, and the surface loop voltage is 0.15 V. We note that if the bootstrap current was large and poorly aligned with the total current, then it would not be possible to achieve these near steady-state conditions. The line-average density is high ($\sim 8 \times 10^{19} \text{ m}^{-3}$) and the $n_e(r)$ profile is relatively flat, characteristic of H modes. The H factor is ~ 2 during the later phase of the discharge, typical of standard ELMing H modes with monotonic q profiles. Because of the high edge density in this discharge, over 50% of the beam power is deposited at $\rho > 0.5$. Our experience to date indicates that enhanced core confinement in the NCS region is not easily achieved unless heating power is more concentrated in the core.

Several key features of the high-performance NCS regime are elucidated by comparing an L-mode NCS discharge 84682 with an H-mode NCS discharge 87072. The temporal evolution of these discharges is compared in Fig. 2. Both have a low target density of $1.3 \times 10^{19} \text{ m}^{-3}$, centrally peaked beam power deposition, and strong core plasma rotation. They begin with $P_{\text{nb}}^{\text{L}} = 5 \text{ MW}$ at 0.3 s into the current ramp and remain in the L mode until the high-power heating phase begins at 1.4 s. Shortly after this time, 87072 is programmed to transition into an ELM-free H mode, while 84682 maintains an L-mode edge until 1.9 s. The early beam power of 5 MW exceeds the H-mode threshold for standard double-null diverted plasmas on DIII-D, so avoiding the H mode in these discharges requires either displacing the plasma toward the upper null (opposite the ion ∇B drift direction) or limiting the plasma on the inner wall.

During the early phase $t < 1.4 \text{ s}$, both discharges show a confinement enhancement factor of $H \sim 1$, which is characteristic of the L-mode regime with monotonic q profiles. During the high-power phase, discharge 84682 shows an increase in H from 1 to 2.5 while still maintaining the L-mode edge. This represents the largest confinement enhancement factor yet observed on DIII-D with an L-mode edge. Peak normalized beta reaches $\beta_N \approx 2.2$ at 1.9 s. Large peaking of the T_i and n_e occurs shortly after the high-power phase begins, resulting in a DD neutron rate of $\Gamma_n \approx 6 \times 10^{15} \text{ n/s}$. Peaking of the density can be seen from the rapid rise in the central channel [Fig. 2(d)] at 1.4 s, while the edge channel [Fig. 2(e)] remains low. The abrupt drops in density are due to short MHD bursts, which will be discussed later.

Discharge 87072 transitions into the H mode at $t = 1.6 \text{ s}$, as seen by the drop in D_α [Fig. 2(b)] and the rapid rate of rise of the edge density [Fig. 2(e)]. An H factor of 3.0 and

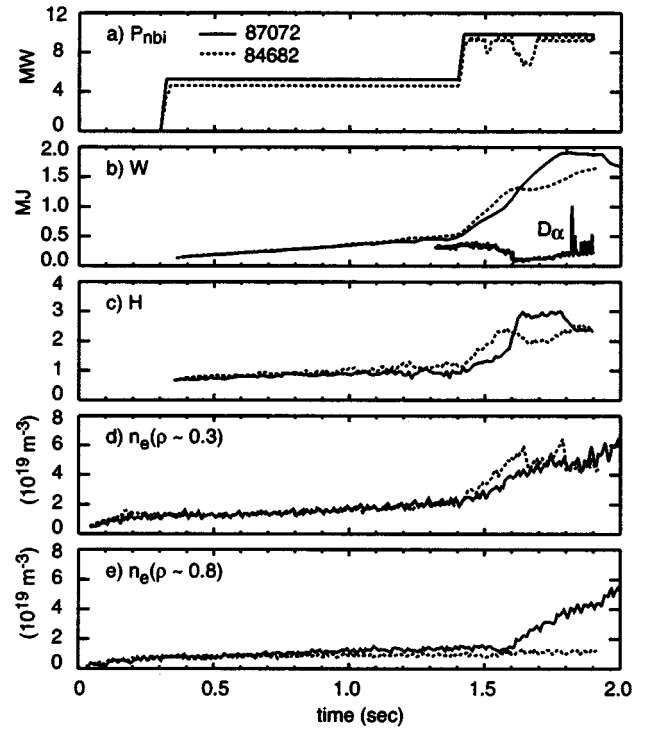


FIG. 2. Time evolution comparison of NCS L- and H-mode discharges 84682 and 87072: (a) neutral beam power, (b) stored energy W , (c) confinement enhancement factor H , (d) electron density near $\rho \sim 0.3$, and (e) electron density near $\rho \sim 0.8$.

$\beta_N \approx 3.2$ is obtained during the ELM-free phase between 1.6 and 1.82 s. The H factor drops to ~ 2.3 when ELMing begins. It is interesting to note that H is similar for the two discharges at 1.9 s, even though the H-mode discharge has improved edge confinement and the L-mode discharge does not.

A comparison of the fitted profiles of $T_e(\rho)$, $T_i(\rho)$, $n_e(\rho)$, and toroidal rotation frequency $\omega_\phi(\rho)$ for these two discharges is shown in Fig. 3. Measurements of T_e and n_e over the range $0.3 < \rho < 1.0$ are provided by Thomson scattering, while electron cyclotron emission and a CO_2 interferometer give additional measurements in the core. A 32 channel charge exchange recombination (CER) system²³ gives T_i , toroidal and poloidal rotation, and carbon impurity density (used for Z_{eff}) measurements. From these profiles the total pressure is calculated using the ONETWO²⁴ transport code, including the effects of neutral beam generated fast ions. The pressure profile is then used, along with MSE and magnetic field measurements, as input to EFIT to reconstruct the $q(r)$ profile shown in Fig. 3. The profiles for the L-mode discharge 84682 are taken at a time when the density peaking is building (1.6 s), while for 87072 we show a time slice approximately 100 ms after the L–H transition. Discharge 84682 shows a large peaking of T_i and n_e , with the radius of maximum ∇T_i and $\nabla \omega_\phi$ localized close to $\rho_{q_{\min}}$ and the radius of maximum ∇n_e localized somewhat inside $\rho_{q_{\min}}$. For 87072, the density profile is flatter, but T_i again shows a rapid increase near $\rho_{q_{\min}}$ similar to the L-mode edge case. The T_e profiles show a small increase in the NCS region for

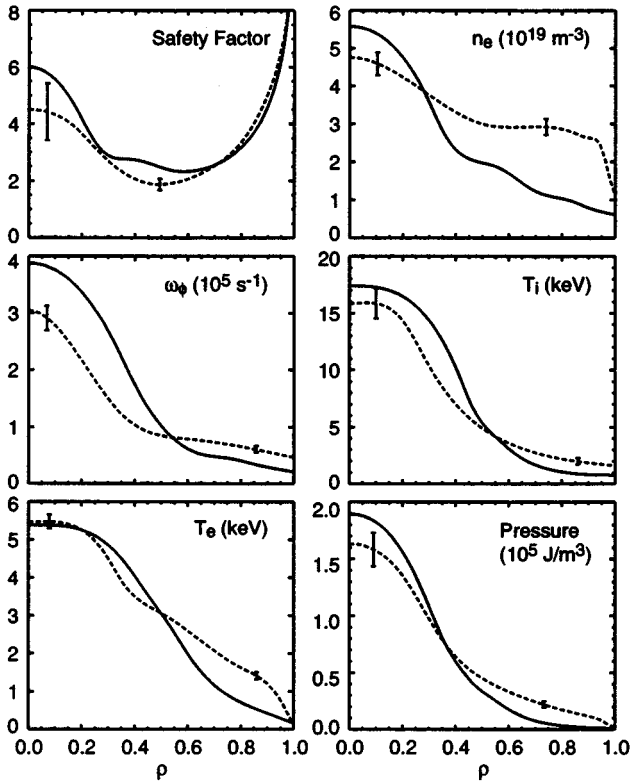


FIG. 3. Comparison of the profiles of $q, n_e, \omega_\phi, T_i, T_e$, and pressure for the L- and H-mode NCS discharges shown in Fig. 2 at 1.6 and 1.7 s, respectively.

both discharges, but the effect is not as dramatic as the other profiles. The strong peaking of T_i with NCS is typical for L- and H-mode discharges, as long as adequate central beam heating is maintained. The density peaking appears to be unique to the L-mode regime, and only appears with $P_{\text{nbi}} \geq 8$ MW.

All of the edge quantities are higher in the H-mode case, resulting in a significantly broader pressure profile, as shown in Fig. 3. We note that as these discharges continue to evolve, the L-mode pressure profile becomes even more peaked due to continued density peaking (until a stability limit is reached), while the H-mode pressure profile becomes broader as the edge density rises and the beam deposition broadens.

These results, plus earlier experimental results from DIII-D^{16,18} and TFTR,¹⁴ indicate that NCS is necessary but not sufficient to achieve enhanced profile peaking and reduced transport in the core. On TFTR, where the enhanced performance is seen primarily as a reduction in particle and ion thermal diffusivity, there appears to be a very clear power threshold at about 18–25 MW. On DIII-D, performance also increases with NBI power, however, a clear and consistent power threshold is difficult to identify. As discussed in Ref. 16, rapid peaking of the ion temperature is often seen in NCS discharges with only 5 MW of early beam power. This transport barrier can develop with no change in P_{nbi} , indicating that the $q(r)$ profile evolution is important. The increase in T_i is almost always seen with $P_{\text{nbi}} > 7$ MW in both the L and

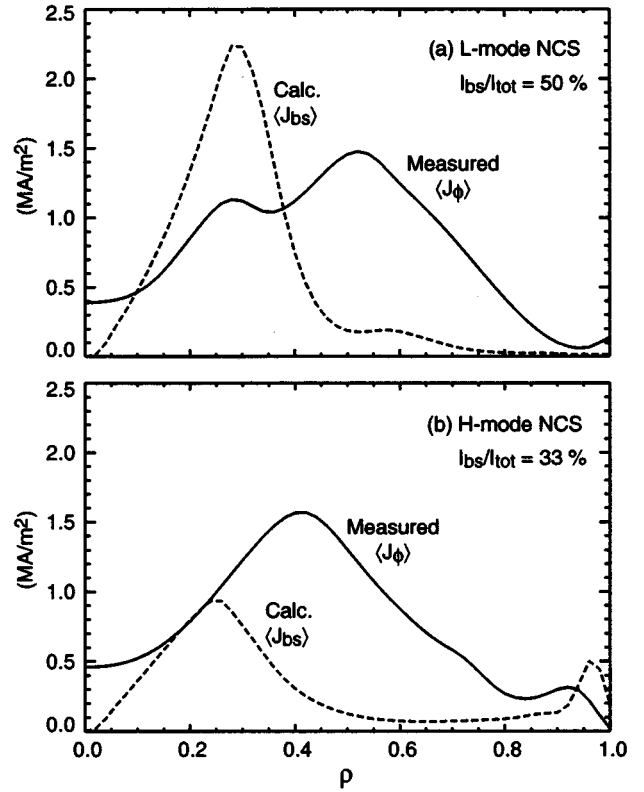


FIG. 4. Comparison of the measured total current density (solid) and calculated ONETWO bootstrap current density (dashed) profiles for the (a) L-mode and (b) H-mode time slices shown in Fig. 3. The L-mode discharge has 75% total noninductive current and the H-mode discharge has 60% noninductive current at these times.

H mode, provided the target density is reasonably low (few $\times 10^{19} \text{ m}^{-3}$). Peaking of the central density is only observed in NCS L-mode discharges for $P_{\text{nbi}} > 8$ MW, as seen in Fig. 2. The H factor in L-mode discharges, while rising slowly during the low power phase, takes a dramatic jump to ~ 2.5 when P_{nbi} is increased. The current working hypothesis on DIII-D is that, in addition to the NCS q profile, $\mathbf{E} \times \mathbf{B}$ flow shear in the core plays an important role in stabilizing turbulence.¹⁹ NCS discharges have strong pressure and ω_ϕ peaking in regions of low poloidal field, which leads to large $E_r/|RB_p|$ shear in the core. The magnitude and radial extent of this shear would be expected to increase with P_{nbi} and may explain the observed power dependence.

III. BOOTSTRAP CURRENT ALIGNMENT

A large bootstrap fraction that is well aligned with the total current is a primary objective of the NCS scenario. Bootstrap current density profiles are calculated for the kinetic profiles shown in Fig. 3 using the ONETWO²⁴ transport code (Hirshman model).²⁵ The results are as shown in Fig. 4. The L-mode case has an approximately 75% noninductive current (beam and bootstrap), peaking at $\rho \sim 0.28$, while the H-mode case has a 60% noninductive current, peaking at $\rho \sim 0.25$. The large bootstrap fraction in the L-mode case is rather remarkable, considering that beta poloidal $\beta_p \sim 0.8$ is lower than the H-mode case, where $\beta_p \sim 1.2$. But because the

bootstrap current scales as $J_{bs} \approx (\epsilon/B_p)(dp/dr)$, we see that large dp/dr in a region of high q (low B_p) can lead to very large bootstrap current densities.

As seen in Fig. 4(a), the calculated bootstrap current for 84682 is peaked at $\rho \approx 0.28$, and is causing a second peak to develop in the measured total current. Earlier in time, before the development of the J_{bs} peak, the measured $\langle J_\phi \rangle$ peaked at $\rho \approx 0.5$ and dropped smoothly toward the magnetic axis. The existence of the J_{bs} peak has also been confirmed by observation of a large depression in the local parallel electric field determined by the time rate of change of MSE B_{vert} measurements.¹⁸ If left in this state for a time comparable to the current diffusion time, the large J_{bs} peak would lead to a decrease in q_{min} and $\rho_{q_{min}}$.

This leads to an important conclusion regarding bootstrap current alignment. The central deposition of P_{nbi} combined with the enhanced core confinement created by the NCS q profile, results in a strongly peaked pressure profile with maximum ∇p and ∇n_e occurring near or inside $\rho_{q_{min}}$. While a peaked pressure profile is advantageous for achieving high reactivity, and high bootstrap fractions, it does not give a well-aligned bootstrap current (with large $\rho_{q_{min}}$) that can be maintained in steady state. A broader pressure profile is more desirable in this respect.

Even though the pressure profile is broader for 87072, J_{bs} is still peaked at too small a radius, as seen in Fig. 4(b). However, the magnitude of peak J_{bs} is closer to the target current density, so the target profile can be maintained for longer durations. An ELMing H mode, such as discharge 83724 shown earlier in Fig. 1, has an even broader pressure profile, and somewhat better bootstrap current alignment (with $I_{Nl}/I_{TOT} \sim 50\%$), as evidenced by the slowly evolving NCS profile. Note that in all these discharges, increased pressure gradient and bootstrap current is required in the region $0.4 < \rho < 0.7$. If further control over the pressure profile can be achieved through control of the $q(r)$ and $\mathbf{E} \times \mathbf{B}$ shear profiles, a more optimized alignment may be obtained.

IV. TRANSPORT ANALYSIS

Transport analysis has been performed using ONETWO for several L-mode discharges that show peaking in both T_i and n_e . We note that the NCS discharges push the validity limit of the standard transport models used in ONETWO in many ways: (1) the core plasma velocity can reach a large fraction of the thermal velocity, which dramatically affects the fast ion slowing down time; (2) low plasma density results in large fast ion populations and charge-exchange power loss; (3) because q is large (low B_{pol}) and ∇T_i is large in the core, the T_i gradient scale length $L_i \equiv T_i / (dT_i/dr)$ becomes comparable to the ion poloidal gyroradius (banana width) $\epsilon^{1/2} \rho_{i\theta}$. Thus, standard neoclassical expressions should be modified in the plasma core. Although the importance of these effects is being evaluated, the transport analysis presented here uses the standard neoclassical models.²⁶

Analysis of reduced transport in the region of NCS is most easily demonstrated in discharges that develop a transport barrier with no change in beam power. An example of such a discharge is shown in Fig. 5(a). Here a rapid rise in

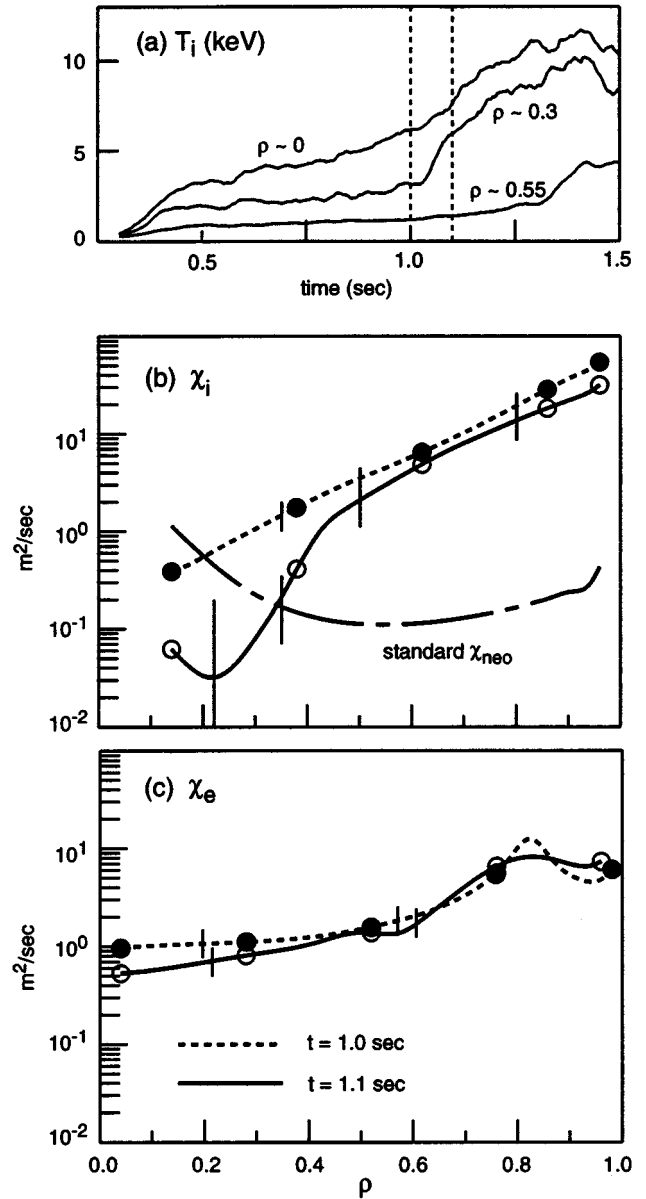


FIG. 5. (a) Time evolution of T_i at three radial locations for an L-mode NCS discharge 84736, showing an improvement in confinement at 1.05 s; (b) ion thermal diffusivity and (c) electron thermal diffusivity before the transition at 1.0 s (dashed) and after the transition at 1.1 s (solid). Neoclassical ion thermal diffusivity is also shown in (b) for comparison.

$T_i(\rho \approx 0.3)$ is observed at 1.05 s with constant $P_{nbi} = 5$ MW. The current ramp for this discharge is complete at 1 s, with $I_p = 1.6$ MA and $B_T = 1.6$ T.

The change in thermal diffusivities χ_i and χ_e across this transition is shown in Figs. 5(b) and 5(c). Empirical thermal diffusivities are calculated from $q_{e,i} = n_{e,i} \chi_{e,i} \partial T_{e,i} / \partial r$, where $q_{e,i}$ is the radial energy flux due to conduction for each species and $r = (\Phi / B_{T_0} \pi)^{1/2}$ where $\Phi =$ toroidal flux. Classical electron-ion energy exchange is assumed and only diagonal transport coefficients are considered. In Fig. 5(b), central χ_i drops by a factor of 10 after the transition to below standard neoclassical values. Here χ_e also shows a drop of $\sim 50\%$, but the drop is probably within statistical uncertainties; also, there may be a systematic un-

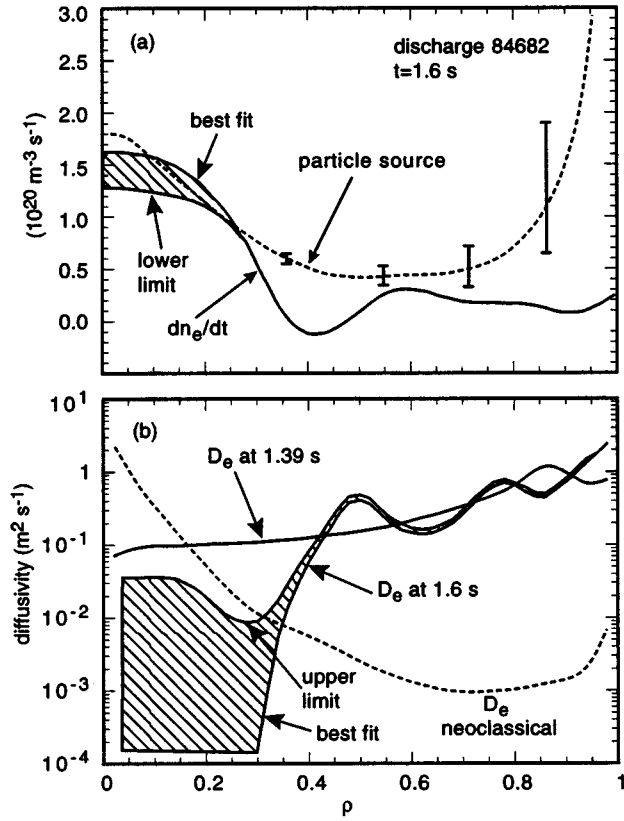


FIG. 6. (a) Source rate and dn_e/dt for the L-mode NCS discharge 84682 at 1.6 s; (b) experimental particle diffusivity D_e before density peaking at 1.39 s and after density peaking at 1.6 s, and neoclassical D_e (dashed). The shaded regions indicate the range of uncertainty due to the lack of Thomson scattering measurements inside $\rho < 0.25$.

certainty in calculating the electron-ion energy exchange. Recent results with direct electron heating using fast wave current drive (FWCD) also indicate about a 50% drop in χ_e with less uncertainty. We note that transport analysis of higher-power discharges, such as those shown in Fig. 2, indicate a much larger drop in χ_i , often going negative. Because of the uncertainties in the models mentioned above, we are continuing an analysis of this result.

Particle diffusion has been analyzed for the L-mode discharge with density peaking shown earlier in Fig. 2. During the density peaking phase, the beam fueling source rate is essentially equal to dn_e/dt , as shown in Fig. 6(a). The error bars in particle source rate were determined by varying the edge fueling rate. The source rate in the core region of interest is unaffected by edge fueling assumptions and is dominated by beam fueling. The uncertainty in the core dn_e/dt (shaded region) is due to the lack of Thomson scattering data inside $\rho \sim 0.25$. The best fit to Thomson and CO_2 interferometer data is shown, along with a lower limit, assuming n_e is flat in the region $0 < \rho < 0.25$.

In Fig. 6(b), the electron particle diffusivity D_e is calculated for an early time with no n_e peaking, and a later time with n_e peaking. Neoclassical diffusivity is shown for comparison. The experimental particle diffusivity is calculated from

$$D_e = \frac{-1}{Hr(\partial n_e / \partial r)} \int_0^r \left(S - \frac{\partial n_e}{\partial t} \right) Hr dr,$$

where S is the electron source and H is a geometric factor. As expected from the particle balance in Fig. 6(a), the particle diffusivity drops to near zero during the density peaking phase. Even the curve labeled upper limit (flat density inside $\rho \sim 0.25$) shows particle diffusivity below neoclassical.

The reduction in core transport in NCS discharges is additionally supported by far-infrared scattering measurements, which indicate a substantial drop in core fluctuations with NCS. We have two working hypotheses to explain the improved confinement.¹⁹ First is stabilization of electrostatic toroidal drift modes by NCS.⁷ Second is increased shear in E_r/RB_p , which is observed in these discharges, and has previously been demonstrated to play a role in the improved confinement observed in the VH mode on DIII-D.²⁷

V. STABILITY

To take full advantage of the NCS configuration, MHD stability must be demonstrated for both ideal ballooning, low- n ideal kink modes, and low- n resistive modes at high β . One key advantage of the NCS configuration is that the plasma is ideally stable to high- n ballooning modes in the region of shear reversal. Ballooning stability has been evaluated using CAMINO²⁸ for typical L- and H-mode NCS discharges. In Fig. 7 we plot $dp/d\rho$ vs ρ for each discharge, along with the calculated region of instability to ideal ballooning. Both discharges have complete second stability access inside $\rho \sim 0.8$. When stability is evaluated for these discharges with a forced monotonic q profile equilibria, they are found to be ballooning unstable. In the L-mode case, this pressure gradient corresponds to a peaked normalized pressure gradient of $\alpha \equiv \mu_0 \sqrt{V} / (2\pi^2 R_0) p'(\psi) V'(\psi) / (2\pi^2) \sim 7.5$, which is the highest value yet observed on DIII-D, and is far beyond the first stability limit. Because of the low-pressure gradient at the edge, the L-mode discharge is well below the region of ballooning instability at the edge. In the H-mode case, the pressure gradient for two times is shown: one early in the ELM-free H-mode period (solid) and one near the termination of the ELM-free period (dashed). The value of $dp/d\rho$ in the core is lower than the L-mode case due to the broader pressure profile, but still exceeds the stability limit that would have existed with a monotonic q profile. Note that the edge value of $dp/d\rho$ rises close to the stability limit near the end of the ELM-free period.

The termination of the high-performance NCS phase of these discharges is distinctly different in the L mode versus the H mode. The L-mode NCS discharges are characterized by large pressure peaking $p(0)/\langle p \rangle \sim 5$ and almost always terminate at $\beta_N \leq 2.3$ in a complete disruption triggered by rapidly growing $m/n=3/1$ or $m/n=2/1$ modes localized in the plasma core. Typical growth times are $\gamma^{-1} = 0.1 - 0.4$ ms, and the mode rotation frequency measured by Mirnov probes matches the core plasma impurity rotation, as measured by CER. Analysis of soft x-ray emission and MSE perturbations indicates the mode is localized near the inside $q=3$ surface, where the magnetic shear is negative.

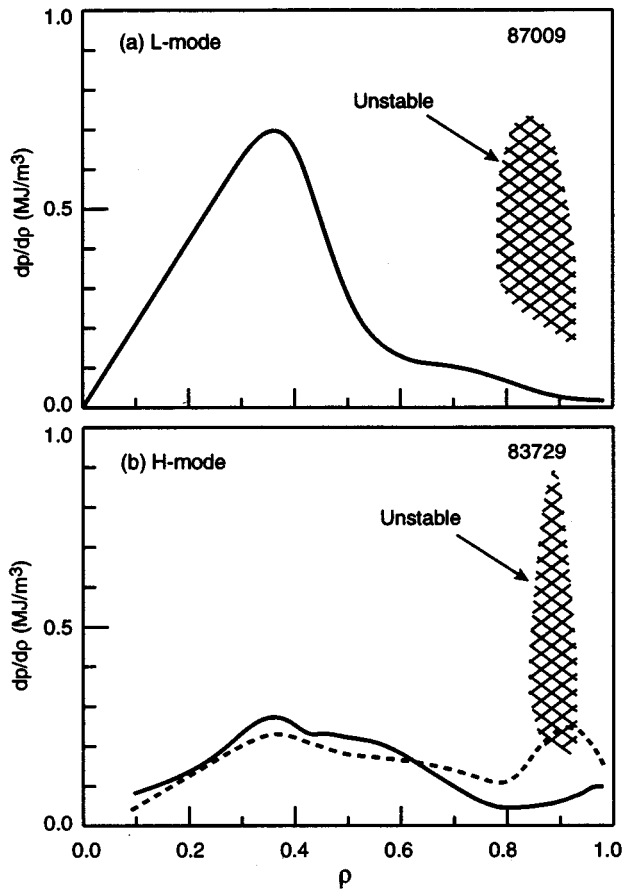


FIG. 7. Ballooning stability analysis for (a) L-mode and (b) H-mode NCS profiles. In (b), the solid curve is early in the ELM-free period and the dashed curve is near the end of the ELM-free period.

The H-mode discharges do not suffer disruptions. Usually the neutron rate and β_N suffer a slow saturation or roll over due to the development of low- n edge kink/ballooning-type MHD, or in some cases Alfvén eigenmodes. These instabilities do not appear to be a consequence of the negative shear, since they are also observed in VH-mode discharges with monotonic q profiles.

The difference in disruptivity between L- and H-mode discharges is illustrated in the Fig. 8 scatter plot, where we plot a density peaking parameter $n_e(\rho \sim 0.3)/n_e(\rho \sim 0.8)$ vs neutron rate Γ_n , at the time of maximum Γ_n . The \times symbols represent discharges with a hard disruption, while the circle symbols denote a soft beta collapse. Most discharges with an n_e peaking factor less than 2 are in the H mode and those greater than 2 are in the L mode. Clearly, the L-mode discharges with large density peaking are highly disruptive. Although pressure peaking is the key parameter here, we chose to plot density peaking because it is the primary difference between the L- and H-mode discharges, and is responsible for the difference in pressure peaking. The few nondisrupting discharges with large density peaking avoided disruption by making a transition to the H-mode shortly after the time slice plotted and evolving to a broader density profile.

One candidate for the cause of the L-mode disruptions is

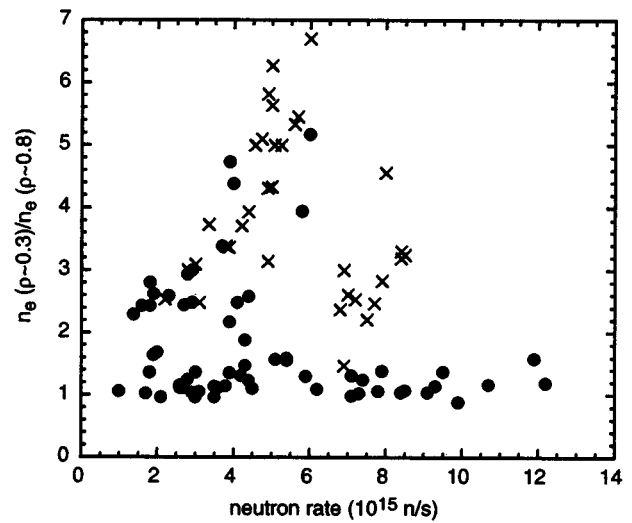


FIG. 8. Density peaking versus neutron rate for many NCS discharges with complete disruptions (\times) and with no disruptions (circle). L-mode NCS discharges generally have peaking factors >2 , while H-mode NCS discharges have peaking factors <2 .

infernal modes triggered when q_{\min} crosses rational values. But we have a large database of discharges, which indicate that the disruptions occur at various values of q_{\min} between 1.5 and 3.0. Furthermore, calculations performed with the ideal MHD stability code GATO,²⁹ indicate that the L-mode discharges are ideally stable. Equilibria for stability calculations are reconstructed using the measured pressure profile, internal field pitch profile (MSE), and external magnetics.

Stability calculations with the linear resistive code MARS³⁰ indicate these discharges are unstable to localized pressure-driven resistive interchange modes,³¹ which are localized to the inner low-order rational q surfaces. The predicted mode number (usually 3/1) and location (inner $q=3$) agree with experimental observations. These modes are defined as resistive interchange in the sense that the parameter D_R [see Eq. (115) in Ref. 31] is positive. Note that for resistive modes, shear stabilization is no longer applicable, since resistivity allows field line reconnection. A more global double tearing mode is also found to be marginally unstable, but can be stabilized by sheared toroidal rotation⁸ and a resistive wall. The local resistive mode is not stabilized by toroidal rotation and is not sensitive to fine details of the q profile. According to MARS calculations, the local mode becomes unstable at $\beta_N \sim 2$, independent of q_{\min} , as q_{\min} is varied from $1.1 \leq q_{\min} \leq 2.7$. However, the mode is found both experimentally and in simulations to be sensitive to the local pressure gradient in the NCS region.

The disruption of L-mode NCS discharges is believed to be a consequence of this resistive interchange. The strong dependence of β_N on pressure peaking and the weak dependence on q_{\min} are consistent with experimental evidence. The growth of the local interchange mode, while not directly responsible for a disruption, can couple to the more global double tearing mode, or to a nearby ideal mode, which is calculated to be unstable when pressure is increased 20% above the experimental value. The local mode is also ob-

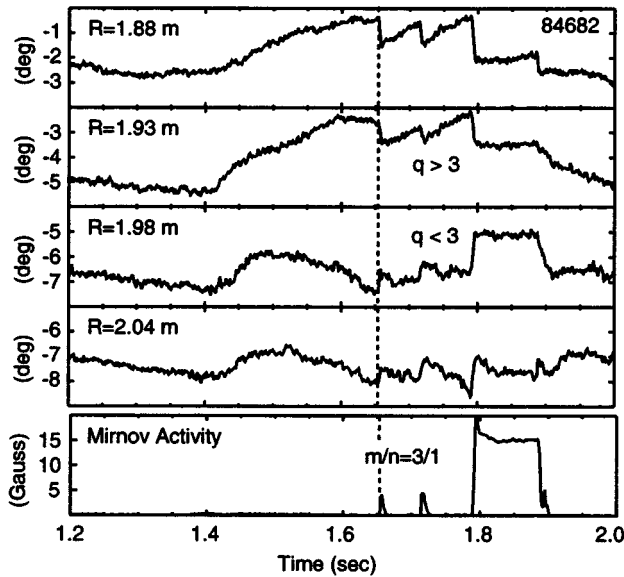


FIG. 9. Time history of MSE signals during MHD activity in an NCS L-mode discharge with highly peaked pressure. An inversion radius is observed at the inner $q=3$ surface where shear is negative.

served to reduce the rotational shear, which tends to destabilize the double tearing mode. The local interchange may also destabilize global modes by local profile modification.

One piece of experimental evidence that strongly supports the resistive mode hypothesis comes from analysis of MHD bursts that often precede the L-mode disruptions. These bursts are observed in most NCS L-mode discharges with peaked pressure. The precursor mode numbers $m/n=3/1$ and growth rates are similar to that of the mode that grows just prior to the disruption. The precursor mode clearly rotates with the rotation of the core plasma, an indication that it is localized in the core. Analysis of soft x-ray emission also indicates the mode is localized inside of $\rho_{q_{\min}}$. From the time history of the MSE pitch angle signals, we note a sawtooth-like step in the poloidal field that is correlated with the MHD burst, as shown in Fig. 9. An inversion radius for the perturbation occurs between channels at $R=1.93$ m and $R=1.98$ m, which lie on either side of the inner $q=3$ surface at this time. Thus, the mode appears to be localized to the inside $q=3$ surface where the negative magnetic shear and pressure gradient are strong.

With this new understanding of the L-mode disruptions, additional experiments were performed to improve plasma performance by programming an H-mode transition to occur before the pressure peaking reaches a critical level. The H-mode transition broadens the pressure profile allowing the discharge to achieve higher β_N . This technique was successful and resulted in DIII-D's highest reactivity discharges with $\Gamma_n=1.2 \times 10^{16}$ n/s.

VI. DISCUSSION

The NCS configuration is a promising regime for improved performance of tokamaks. Robust and reliable formation of the NCS profile has been demonstrated using early

TABLE I. Record DIII-D parameters obtained in NCS discharges.

DD neutron rate Γ_n	1.2×10^{16} n/s
$T_i(0)$	22.5 keV
Toroidal plasma rotation frequency f_Ω	60 kHz ($v_\phi=650$ km/s)
$T_e(0)$ with FWCD	8 keV
Pressure peaking $p(0)/\langle p \rangle$	5.0
H factor with L-mode edge	2.5
Normalized pressure gradient α	7.5

beam injection in DIII-D discharges. DIII-D record values of many important parameters have been obtained in NCS discharges, and are summarized in Table I. The peak ion temperature of 22.5 keV is just slightly above that previously high obtained in a hot-ion VH mode, but with NCS the ion temperature remains high over a broader region of the core inside of $\rho \leq 0.3$. This gives higher plasma reactivity in NCS discharges, with both L-mode and H-mode edge conditions, and has led to a 70% increase in deuterium–deuterium (DD) reactivity over the previous highest value obtained in the hot-ion VH mode—a clear indication of the increased performance potential.

The increased performance in the NCS regime is a consequence of the formation of a transport barrier in the region of shear reversal. With sufficient heating power there is a clear increase in central T_i , with a corresponding drop in χ_i to near or below standard neoclassical levels. Direct electron heating with FWCD shows a similar increase in central T_e and a corresponding drop in χ_e by 50%. In discharges with an L-mode edge, clear density peaking is observed, giving a particle diffusivity near or below neoclassical values.

The peaked pressure profiles that result in NCS discharges with an L-mode edge give high reactivity and high bootstrap current ($\sim 50\%$), but have serious limitations. First, J_{bs} is peaked at a location inside $\rho_{q_{\min}}$ and is significantly larger than the target current density. In a longer pulse, this would lead to a decrease in q_{\min} and $\rho_{q_{\min}}$, and an eventual collapse of the NCS profile.

Low β limits constitute the second limitation of the strongly peaked pressure profiles. Experimentally, $\beta_N \leq 2.3$ is observed with strong pressure peaking of $p(0)/\langle p \rangle \sim 5$. This limit is independent of the details of the q profile, and is consistent with the resistive interchange mode, which is driven by the pressure peaking. The reduced stability limit and the unfavorable bootstrap current alignment will make developing high-performance steady-state scenarios with peaked pressure profiles extremely challenging.

The H-mode NCS configuration provides some improvement. The highest DD reactivity of 1.2×10^{16} n/s and NCS normalized beta $\beta_N \sim 4.2$ have been obtained in this regime. The peak in J_{bs} is still localized to a radius inside of $\rho_{q_{\min}}$, but is sufficiently close to the target not to cause a rapid collapse. The steep edge pressure gradient and resultant bootstrap current are destabilizing to the edge kink, which leads to a more gentle β collapse. Active means to control this steep gradient are under investigation at DIII-D.

Improved control of the pressure profile is the next step toward developing steady-state high-performance NCS scenarios. Increased pressure gradient in the region of $0.5 < \rho$

<0.8 is required for improved bootstrap alignment. Different heating, momentum, and particle sources may contribute to improved control. Also, we propose that the pressure gradient can be moved out by increasing the radius of q_{\min} using noninductive current drive sources.

The negative central magnetic shear regime has led to a substantial increase in plasma performance on DIII-D in a short time with limited experimental effort. We believe this regime holds great promise for steady-state high-performance tokamaks.

ACKNOWLEDGMENTS

The authors would like to acknowledge the continued encouragement and support from V. S. Chan and T. C. Simonen. We also thank the Thomson scattering group for providing high-quality temperature and density data.

This is a report of work supported by the U.S. Department of Energy under Contracts No. DE-AC03-89ER51114, No. W-7405-ENG-48, No. DE-AC05-84OR21400, and Grants No. DE-FG02-89ER53297, No. NDE-FG05-86ER5, and No. DE-FG03-86ER53266.

¹T. S. Taylor, H. St. John, A. D. Turnbull, Y. R. Lin-Liu, K. H. Burrell, V. S. Chan, M. S. Chu, J. R. Ferron, L. L. Lao, R. J. La Haye, E. A. Lazarus, R. L. Miller, P. A. Politzer, D. P. Schissel, and E. J. Strait, *Plasma Phys. Controlled Fusion* **36**, B229 (1994).
²R. J. Goldston, S. H. Batha, R. H. Bulmer, D. N. Hill, A. W. Hyatt, S. C. Jardin, F. M. Levinton, S. M. Kaye, C. E. Kessel, E. A. Lazarus, J. Manickam, G. H. Neilson, W. M. Nevins, L. J. Perkins, G. Rewoldt, K. I. Thomassen, and M. C. Zarnstorff, *Plasma Phys. Controlled Fusion* **36**, B213 (1994).
³A. D. Turnbull, T. S. Taylor, Y. R. Lin-Liu, and H. St. John, *Phys. Rev. Lett.* **74**, 718 (1995).
⁴J. Manickam, M. S. Chance, S. C. Jardin, C. Kessel, D. Monticello, N. Phomphrey, A. Reiman, C. Wang, and L. E. Zakharov, *Phys. Plasmas* **1**, 1601 (1994).
⁵C. Kessel, J. Manickam, G. Rewoldt, and W. M. Tang, *Phys. Rev. Lett.* **72**, 1212 (1994).
⁶B. B. Kadomtsev and O. P. Pogutse, *Sov. Phys. JETP* **24**, 1172 (1967).
⁷G. Rewoldt, W. M. Tang, and M. S. Chance, *Phys. Fluids* **25**, 480 (1982).
⁸M. S. Chu, J. M. Greene, T. H. Jensen, R. L. Miller, A. Bondeson, R. W. Johnson, and M. E. Mauel, *Phys. Plasmas* **2**, 2236 (1995).
⁹E. A. Lazarus, L. L. Lao, T. H. Osborne, T. S. Taylor, A. D. Turnbull, M. S. Chu, A. G. Kellman, E. J. Strait, J. R. Ferron, R. J. Groebner, W. W. Heidbrink, T. N. Carlstrom, F. J. Helton, C. L. Hsieh, S. Lippmann, D. P. Schissel, R. T. Snider, and D. Wroblewski, *Phys. Fluids B* **4**, 3644 (1992).
¹⁰M. Hugon, B. Ph. van Milligen, P. Smeulders, L. C. Appel, D. V. Bartlett, D. Boucher, A. W. Edwards, L.-G. Eriksson, C. W. Gowers, T. C. Hender, G. Huysmans, J. J. Jacquinet, P. Kupschus, L. Porte, P. H. Rebut, D. F. J. Start, F. Tibone, B. J. D. Tubbing, M. L. Watkins, and W. Zwingmann, *Nucl. Fusion* **32**, 33 (1992).
¹¹G. T. Hoang, C. Gil, E. Joffrin, D. Moreau, A. Becoulet, P. Bibet, J. P. Bizarro, R. V. Bundy, J. Carrasco, J. P. Coulon, C. De Michelis, T. Dudok De Wit, P. Monier-Garbet, M. Goniche, R. Guirlet, T. Hutter, S. M. Kaye, J. Lasalle, L. Laurent, P. Lecoustey, X. Litaudon, M. Mattioli, Y. Peysson, A.-L. Pecquet, G. Rey, S. A. Sabbagh, B. Saoutic, G. Tonon, and J. C. Vallet, *Nucl. Fusion* **34**, 75 (1994).
¹²Y. Kamada, K. Ushigusa, O. Naito, Y. Neyatani, T. Ozeki, K. Tobita, S. Ishida, R. Yoshino, M. Kikuchi, M. Mori, and H. Ninomiya, *Nucl. Fusion* **34**, 1605 (1994).
¹³J. L. Luxon, R. Anderson, F. Batty, C. B. Baxi, G. Bramson, N. H. Brooks, B. Brown, B. Burley, K. H. Burrell, R. Callis, G. Campbell, T. N. Carl-

strom, A. P. Colleraine, J. Cummings, L. Davis, J. C. DeBoo, S. Ejima, R. Evanko, H. Fukumoto, R. Gallix, J. Gilleland, T. Glad, P. Gohil, A. Gootgeld, R. J. Groebner, S. Hanai, J. Haskovec, E. Heckman, M. Heilberger, F. J. Helton, N. Hosogane, C.-L. Hsieh, G. L. Jackson, G. Jahns, G. Janeschitz, E. Johnson, A. G. Kellman, J. S. Kim, J. Kohli, A. Langhorn, L. L. Lao, P. Lee, S. Lightner, J. Lohr, M. A. Mahdavi, M. Mayberry, B. McHarg, T. McKelvey, R. Miller, C. P. Moeller, D. Moore, A. Nerem, P. Noll, T. Ohkawa, N. Ohyabu, T. H. Osborne, D. O. Overskei, P. I. Petersen, T. W. Petrie, J. Phillips, R. Prater, J. Rawls, E. E. Reis, D. Remsen, P. Riedy, P. Rock, K. Schaubel, D. P. Schissel, J. T. Scoville, J. P. Smith, Jr., P. Smith, T. Smith, R. T. Snider, R. D. Stambaugh, R. Stav, H. St. John, R. E. Stockdale, E. J. Strait, R. Street, T. S. Taylor, J. Tooker, M. Tupper, S. K. Wong, and S. Yamaguchi, *Plasma Physics and Controlled Nuclear Fusion Research 1986* (International Atomic Energy Agency, Vienna, 1987), Vol. 1, p. 159.
¹⁴F. M. Levinton, M. C. Zarnstorff, S. H. Batha, M. Bell, R. E. Bell, R. V. Budny, C. Bush, Z. Chang, E. Fredrickson, A. Janos, J. Manickam, A. Ramsey, S. A. Sabbagh, G. L. Schmidt, E. Synakowski, and G. Taylor, *Phys. Rev. Lett.* **75**, 4417 (1995).
¹⁵B. W. Rice, T. S. Taylor, K. H. Burrell, T. A. Casper, C. B. Forest, H. Ikezi, L. L. Lao, E. A. Lazarus, M. E. Mauel, B. W. Stallard, and E. J. Strait, "The formation and evolution of negative central shear current profiles in the DIII-D tokamak," to appear in *Plasma Phys. Controlled Fusion*.
¹⁶E. J. Strait, L. L. Lao, M. E. Mauel, B. W. Rice, T. S. Taylor, K. H. Burrell, M. S. Chu, E. A. Lazarus, T. H. Osborne, S. J. Thompson, and A. D. Turnbull, *Phys. Rev. Lett.* **75**, 4421 (1995).
¹⁷P. N. Yushmanov, T. Takizuka, K. S. Riedel, O. J. W. F. Kardaun, J. G. Cordey, S. M. Kaye, and D. E. Post, *Nucl. Fusion* **30**, 1999 (1990).
¹⁸B. W. Rice, E. A. Lazarus, M. Austin, K. H. Burrell, T. A. Casper, R. J. Groebner, P. Gohil, C. B. Forest, H. Ikezi, L. L. Lao, M. E. Mauel, G. Navratil, B. W. Stallard, E. J. Strait, and T. S. Taylor, "Observations of enhanced core confinement in negative magnetic shear discharges with an L-mode edge on DIII-D," to appear in *Nucl. Fusion*.
¹⁹L. L. Lao, K. H. Burrell, T. S. Casper, V. S. Chan, M. S. Chu, J. C. DeBoo, E. J. Doyle, R. D. Durst, C. B. Forest, C. M. Greenfield, R. J. Groebner, F. L. Hinton, Y. Kawano, E. A. Lazarus, Y. R. Lin-Liu, M. E. Mauel, W. H. Meyer, R. L. Miller, G. A. Navratil, T. H. Osborne, Q. Peng, C. L. Rettig, G. Rewoldt, T. L. Rhodes, B. W. Rice, D. P. Schissel, B. W. Stallard, E. J. Strait, W. M. Tang, T. S. Taylor, A. D. Turnbull, R. E. Waltz, and the DIII-D Team, *Phys. Plasmas* **3**, 1951 (1996).
²⁰L. L. Lao, J. R. Ferron, R. J. Groebner, W. Howl, H. St. John, E. J. Strait, and T. S. Taylor, *Nucl. Fusion* **30**, 1035 (1990).
²¹D. Wroblewski and L. L. Lao, *Rev. Sci. Instrum.* **63**, 5140 (1992).
²²B. W. Rice, D. G. Nilson, and D. Wroblewski, *Rev. Sci. Instrum.* **66**, 373 (1995).
²³P. Gohil, K. H. Burrell, R. J. Groebner, E. McKee, and R. P. Seraydarian, in *Proceedings of the 14th IEEE/NPSS Symposium on Fusion Technology* (Institute of Electrical and Electronics Engineers, New York, 1992), Vol. II, p. 1199.
²⁴See National Technical Information Service Document No. GA-A16178 (W. W. Pfeiffer, R. H. Davidson, R. L. Miller, and R. E. Waltz, "ONETWO: A computer code for modeling plasma transport in tokamaks," General Atomics Report GA-A16178, 1980). Copies may be ordered from the National Technical Information Service, Springfield, Virginia 22161.
²⁵S. P. Hirshman, *Phys. Fluids* **21**, 1295 (1978).
²⁶F. L. Hinton and R. D. Hazeltine, *Rev. Mod. Phys.* **48**, 239 (1976).
²⁷K. H. Burrell, E. J. Doyle, P. Gohil, R. J. Groebner, J. Kim, R. J. La Haye, L. L. Lao, R. A. Moyer, T. H. Osborne, W. A. Peebles, C. L. Rettig, T. H. Rhodes, and D. M. Thomas, *Phys. Plasmas* **1**, 1536 (1994).
²⁸M. S. Chance, in *Proceedings of Theory of Fusion Plasma*, Varenna, 1987 (Societa Italiana di Fisica, Bologna, Italy, 1988), Vol. 18, p. 87.
²⁹L. C. Bernard, F. J. Helton, and R. W. Moore, *Comput. Phys. Commun.* **24**, 377 (1981).
³⁰A. Bondeson, G. Vlad, and H. Lutjens, *Phys. Fluids B* **4**, 1889 (1992).
³¹A. H. Glasser, J. M. Greene, and J. L. Johnson, *Phys. Fluids* **18**, 875 (1975).